Topology of DNA G-Quadruplexes Can Be Harnessed in Holliday Junction-Based DNA Suprastructures to Control and Optimize Their Biocatalytic Properties

Dehui Qiu, Mingpan Cheng, Petr Stadlbauer, Jielin Chen, Michal Langer, Xiaobo Zhang, Qiang Gao, Huangxian Ju, Jiří Šponer, Jean-Louis Mergny, et al.

Topology of DNA G-Quadruplexes Can Be Harnessed in Holliday Junction-Based DNA Suprastructures to Control and Optimize Their Biocatalytic Properties

Dehui Qiu,◆ Mingpan Cheng,◆ Petr Stadlbauer,*,◆ Jielin Chen, Michal Langer, Xiaobo Zhang, Qiang Gao, Huangxian Ju, Jiří Šponer, Jean-Louis Mergny, David Monchaud,* and Jun Zhou*

ABSTRACT: The nature, composition, and topology of the active sites of both natural and artificial enzymes are key determinants of their catalytic performance. While interesting structural insights have been obtained for natural enzymes (e.g., horseradish peroxidase, HRP), the accurate catalytic microenvironment of HRP-mimicking DNA-based catalysts known as G-quadruplex (GQ)/hemin DNAzymes is still unclear. Herein, we report on a strategy allowing for fully controlling the nature of the active site of GQ DNAzyme, precisely manipulating the composition and topology of the hemin (Fe(III)-protoporphyrin IX) cofactor binding site. This was achieved by introducing GQ within a Holliday junction (HJ) suprastructure that enables to seize control of both the GQ folding topology (parallel, antiparallel, hybrid) and the GQ strand directionality (clockwise, counter-clockwise). By doing so, we demonstrate that the different GQ topologies are equivalent for both hemin binding and activation and that the flanking nucleotides (dA or dTC) modulate the activation of hemin in a GQ topology-dependent manner. Our experimental findings are supported by the most extensive molecular dynamics simulations ever been done on GQ DNAzyme, thus providing unique mechanistic insights into the biocatalytic activity of GQs.

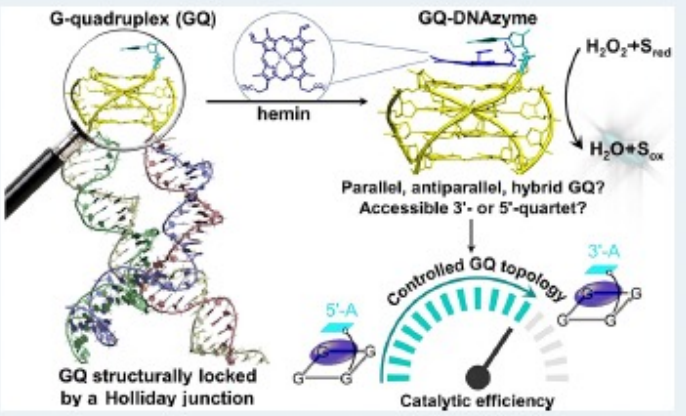

KEYWORDS: *G-quadruplex, DNAzyme, Holliday junction, molecular dynamics simulations, catalytic mechanism*

INTRODUCTION

DNA-based enzymes (known as DNAzymes) have experienced a considerable development since their initial discovery via in vitro selection experiments in 1994.[1] A DNAzyme usually consists of a DNA sequence that folds into a special secondary structure prone to accommodate a metallic cofactor and a substrate, which makes the resulting DNA/cofactor complex catalytically competent, able to assist a broad variety of chemical reactions.[2−4] DNA G-quadruplexes (GQs) are such a secondary structure: GQs are formed by guanine (G)-rich sequences through the stacking of several G-quartets, a macrocyclic array of four Gs associated by Hoogsteen hydrogen bonds (Figure 1A,B).[5] GQs are popular scaffolds for DNAzymes as their three-dimensional structure makes them prone to interact strongly with metallic cofactors (mostly atop their accessible G-quartet), notably hemin (or Fe(III)-protoporphyrin IX). The resulting GQ/hemin complex was shown to accelerate several types of chemical reactions,[4] although through a mechanism that remains to be fully uncovered (vide infra).[6]

It is now established that the topology of a GQ strongly influences its biocatalytic properties.[4,5] However, the factors that control GQ topology, including flanking tails, loops, and G-quartet modification, and the way they influence the catalytic performance of the resulting GQ/hemin DNAzymes is not yet fully understood. Over the past years, a series of rules have emerged: (1) a GQ that adopts a parallel topology (i.e., with all the strands oriented in the same direction) is more catalytically competent than a GQ with either a hybrid topology (i.e., with one strand pointing in the opposite direction to the three others) or an antiparallel topology (with two pairs of strands oriented in an opposite direction);[7−10] (2) the addition of flanking nucleotides (e.g., d(CCC) at either 5′ or 3′ ends of GQs,[11] d(A)[12−15] or d(TC)[14,16,17] at the 3′ end)

Received: June 20, 2023
Revised: July 5, 2023

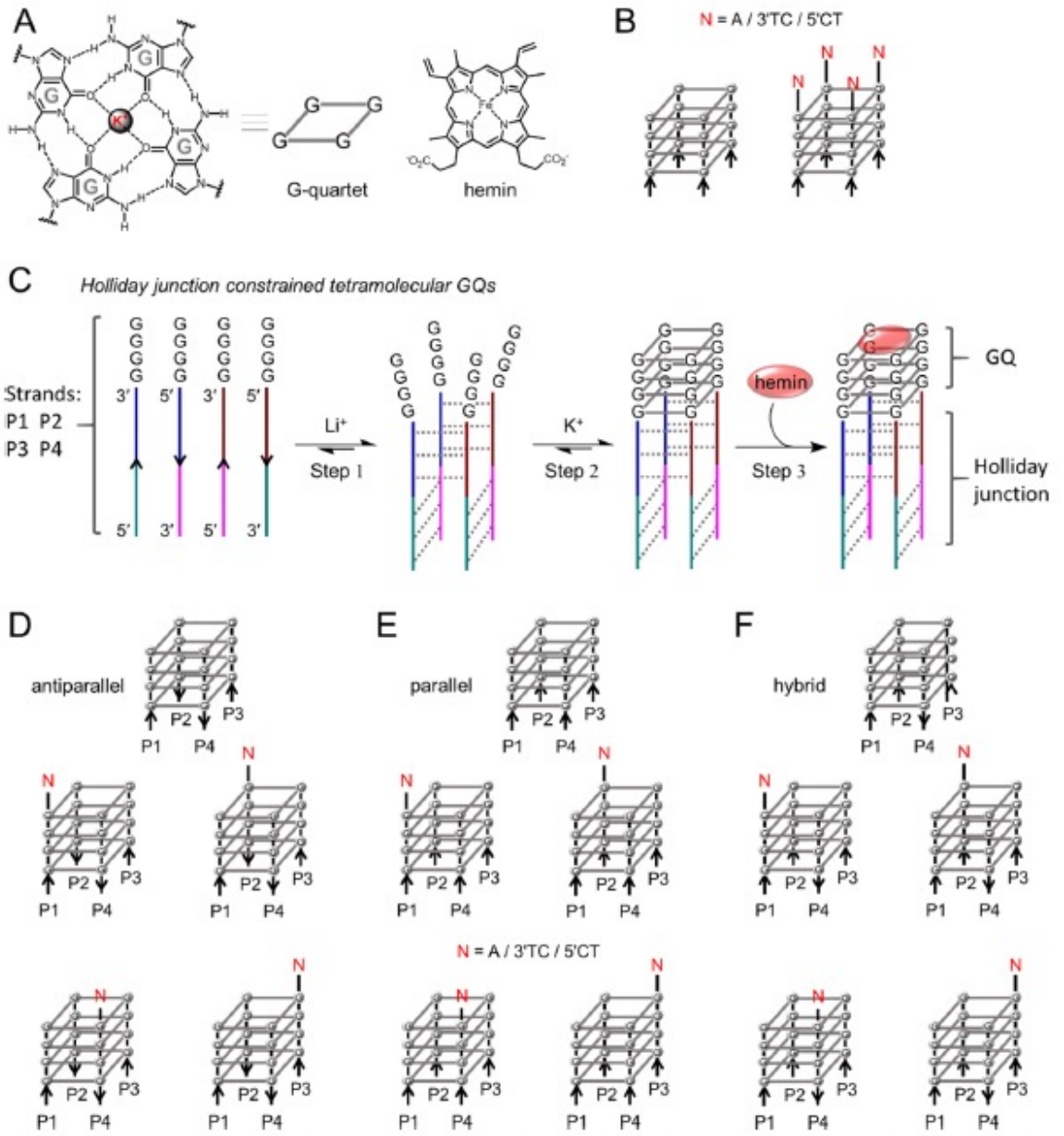

Figure 1. Schematic representation of the constructs used in this study: (A) Structure of a G-quartet and chemical structure of hemin. (B) Schematic representation of classical tetramolecular GQs; arrows indicate the 5′ to 3′ strand direction of the G-tracts. (C) Construction of a HJ-constrained GQ: Step 1, the HJ structure is assembled in the presence of lithium ions; Step 2, the GQ is folded upon the addition of K^+ ions; Step 3, the DNAzyme is formed by the addition of hemin. (D–F) HJ-constrained GQs with (D) antiparallel, (E) parallel, and (F) hybrid conformations. Schematic representation of 9 different d(A), d(TC), or d(CT) tails at the solvent-accessible terminal G-quartet in each type of GQ. Composition of all different assemblies is shown in Tables S1 and S2.

enhances the catalytic properties of GQs; (3) the modification of the base composition of the middle loop[18−20] regulates the enzymatic activity of the resulting GQ; (4) the addition of either an extra GQ unit[21−24] or a substrate aptamer[25−27] also improves catalytic performance of the resulting constructs; and finally, (5) the chemical modifications of Gs[14,28] involved in the G-quartet were also found to affect the activity of DNAzymes. These studies highlight the key roles that the microenvironment of the hemin binding site plays on the performance of GQ DNAzymes. However, a systematic investigation of all these parameters is still required to better understand them.

In this work, we precisely manipulate the hemin binding pocket within a GQ inserting it in a Holliday junction (HJ)-based suprastructure[29,30] (Figure 1). In doing so, we found that the binding and activation of hemin are rather unexpectedly independent on the GQ topology but also that the 3′-nucleotide overhang (either d(A) or d(TC)) exercise a significant influence over biocatalysis in a GQ topology-dependent manner. We finally show that varying the HJ length can be used to control the strand progression directionality in the GQ structure, affecting the positions of bases near the active site.

RESULTS

Constructs of G-Quadruplex Structures. The usual, so called "free" tetramolecular GQs (in comparison with HJ-constrained tetramolecular GQs described herein) suffer from several limitations (Figure 1B): (1) the four strands nearly always associate into a parallel GQ topology, that is, with an identical strand direction; (2) the flanking sequences, in close proximity to solvent-exposed G-quartets, are either absent (Figure 1B, left) or identical at the four extremities as a result of the strand direction (Figure 1B, right); and (3) the two solvent-exposed G-quartets at 5′ and 3′ ends have both the

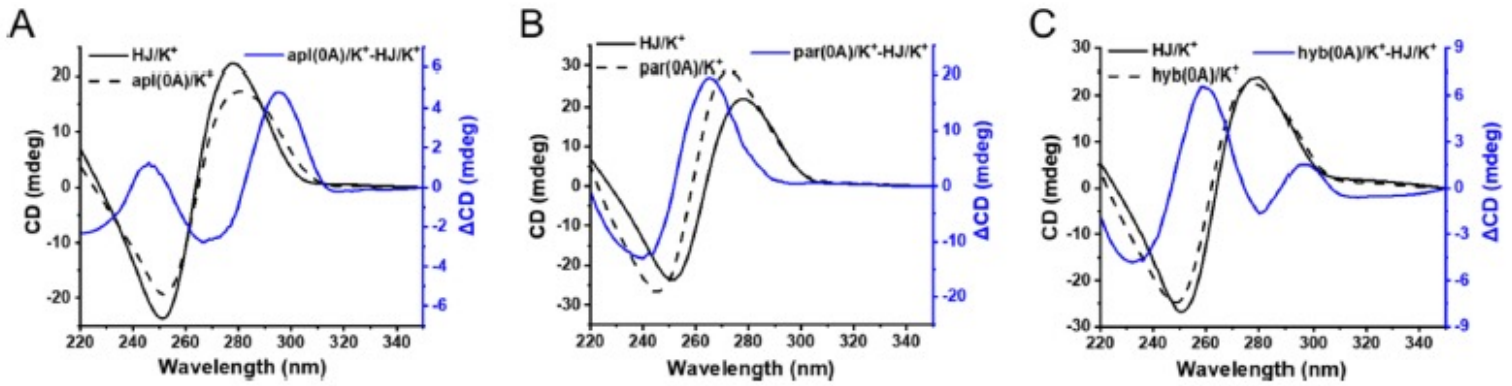

Figure 2. Circular dichroism (CD) investigations: HJ CD signal is shown as a black solid line, that of the HJ-GQ assemblies in black dashed line, i.e., (A) **apl(0A)**, (B) **par(0A)**, and (C) **hyb(0A)**. The difference CD spectra are shown in blue (right vertical axis).

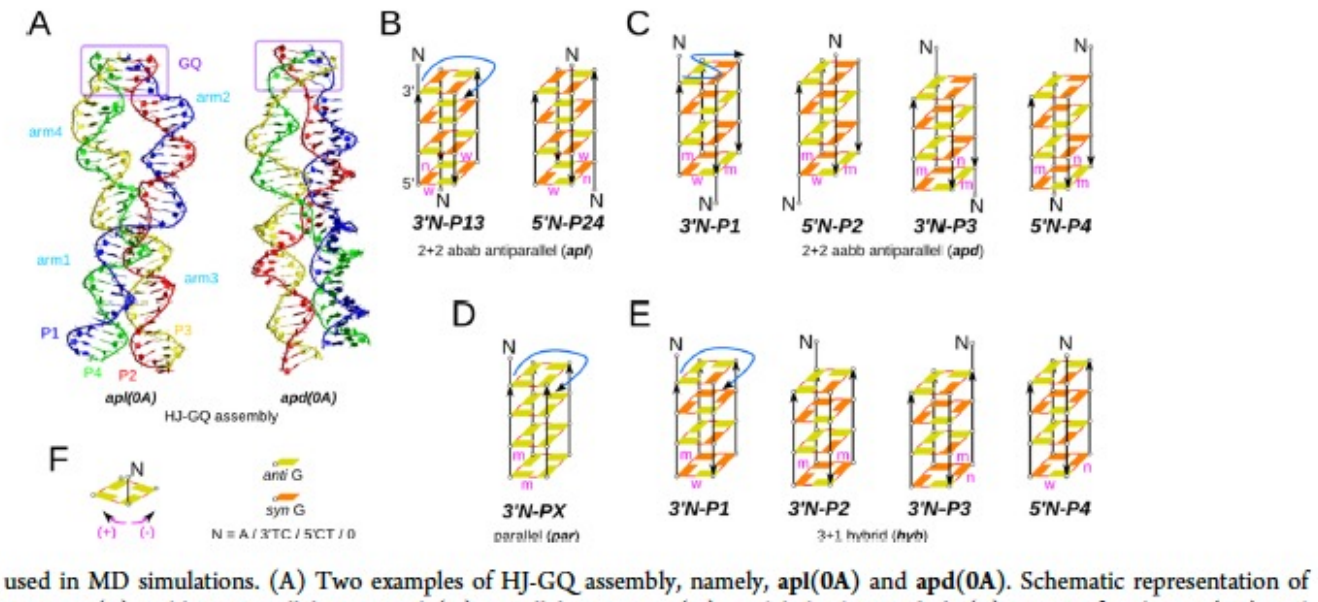

Figure 3. Models used in MD simulations. (A) Two examples of HJ-GQ assembly, namely, **apl(0A)** and **apd(0A)**. Schematic representation of abab antiparallel GQs **apl** (B), aabb antiparallel GQs **apd** (C), parallel GQs **par** (D), and hybrid GQs **hyb** (E); except for the **apl(0A)** and **apd(0A)** models, the GQ models were simulated without HJ to increase computational efficiency (see Methods). The (+) and (−) notation in (F) indicates groove's relative position with respect to the terminal G-quartet and flanking nucleotide(s) N (either d(A) on either end, d(TC) on 3′-end, d(CT) on 5′-end, or no flanking nucleotide (labeled "0"). The blue arrows indicate the clockwise progression of strands P1-P2-P3-P4 in **apl**, **par** and **hyb**, and ⅄-like progression in **apd**. The purple letters indicate groove type adjacent to strands with flanking nucleotides (m, n, and w stand for medium, narrow, and wide, respectively).

ability to bind hemin, which complicates the study of the effects of the cofactor binding site on DNAzymes activity.

By taking advantage of the spatial constraint introduced by the HJ (Figure 1C), several structural regulations of the GQs could be uniquely achieved: (1) the tetramolecular GQs can have different conformations: antiparallel (or **apl**) when P1 and P3 G-tracts point in the same direction, while P2 and P4 are in the opposite orientation (Figure 1D); parallel (or **par**), thanks to the incorporation of two inverted G-tracts at the P2 and P4 strands (see Table S1 for details), which makes the four G-tracts pointing in the same directions (Figure 1E); and hybrid (or **hyb**) with one inverted G-tract in the P2 strand, which makes P4 adopting a reverse direction as compared to the three other G-tracts (Figure 1F); (2) a single dA or dTC (i.e., 3′-dTC or 5′-dCT) tail, known to enhance the GQ DNAzyme activity,[12,16,17] could be introduced at any desired position, i.e., at the end of any of the four strands in a controllable manner; and (3) one terminal G-quartet is sterically hindered as a result of the high steric constraint imposed by the HJ structure, which mainly drives hemin to the other G-quartet. All these features allow to precisely control the nature of the GQ hemin pocket and thus how it modulates the activity of the GQ/hemin DNAzyme.

The 22 assemblies (21 HJ-GQ assemblies plus the naked HJ as control) discussed and used herein are listed in Tables S1 and S2. The formalism used should be read as follows: **apl(0A)** stands for an antiparallel GQ constrained by an HJ with no base modification at the ends; **apl(3′A-P1)** represents an antiparallel GQ with a dA tail located at the 3′ end of the P1 strand; **hyb(3′A-P2)** represents a hybrid GQ with a dA tail located at the 3′ end of the P2 strand (Figure 1F).

HJ-GQ Assembly. The formation of GQs constrained by HJ was first validated by a series of biophysical assays including isothermal difference spectra (IDS)[31] on the basis of the mathematical difference between the absorbance spectra from unfolded and folded oligonucleotides, obtained in the absence and presence of KCl at 25 °C, respectively. The signatures (Figures S1 and S2) display typical negative and positive peaks around 295 and 245 nm, respectively, indicating the formation of a GQ structure.[14,32,33] The lack of characteristic IDS peaks for HJ alone confirms that no GQ is formed from this construct, as expected. In order to confirm this, circular dichroism (CD) spectra of the GQ core were calculated by subtracting the spectra of HJ in K^+ from the spectra of the full assembly in K^+. The CD difference spectra (Figure 2, blue curves, right vertical axis) confirm the antiparallel nature of

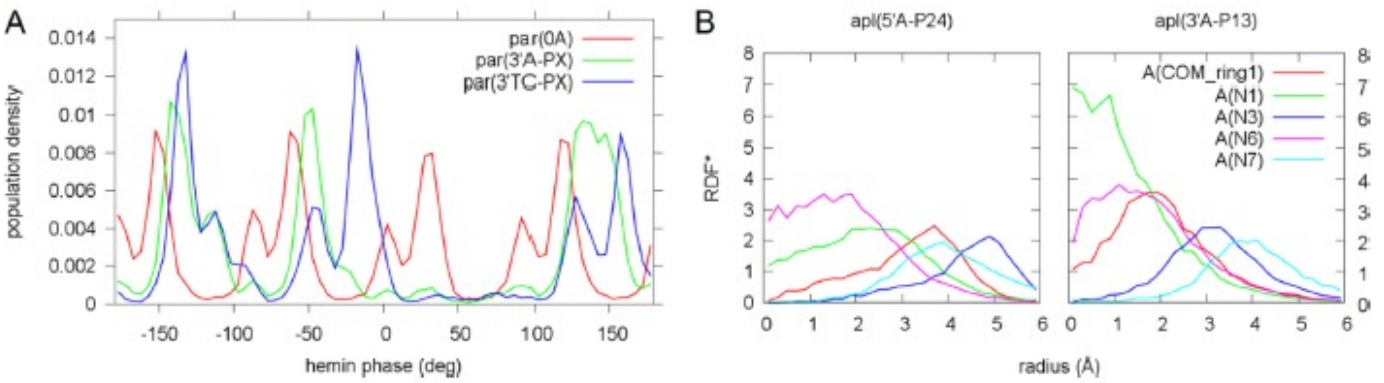

Figure 4. Interaction of hemin with GQs. Hemin rotation phase distribution (A) reflects the four-fold symmetry of ***par(0A)***; in ***par(3′A-PX)*** and ***par(3′TC-PX)***, the flanking nucleotide(s) interferes with the interaction of hemin with the GQ backbone, so one peak is missing. Interaction of d(A) with hemin described by RDF* reveals differences between ***apl(3′A-P24)*** and ***apl(3′A-P13)*** (B); in the former, the iron is mostly in contact with d(A)'s amino group (N6), while the pyrimidine ring N1 atom is preferred in the latter. "COM_ring1" stands for the center of mass of the pyrimidine ring. Hemin rotation phase and RDF* are described in detail in the Supporting Information.

apl(0A) (negative and positive peaks at 265 and 295 nm, respectively; Figure 2A), the parallel nature of **par(0A)** (negative and positive peaks at 240 and 265 nm, respectively; Figure 2B), and the hybrid nature of **hyb(0A)** (a negative peak at 235 nm, two positive peaks at 260 and 295 nm; Figure 2C).[34] The CD for other constrained GQs (Figure S3) also confirm the GQ fold within the resulting assemblies.

The thermal stability of the assemblies in either Li^+-rich buffer or Li^+-/K^+-rich buffer was investigated by monitoring the absorbance at 260 nm upon temperature increase from 5 to 95 °C. Mid-transition temperatures ($T_{1/2}$) were calculated from the UV-melting profiles seen in Figure S4. Upon addition of K^+, $T_{1/2}$ values for HJ alone increased from 62 to 66 °C, due to the increase in ionic strength (Figure S4A,C). The UV-melting profiles of **apl(0A)** in the absence and presence of K^+ can be seen in Figure S4B: in the absence of K^+, the one-stage melting curve led to a $T_{1/2}$ value of 59 °C; in the presence of K^+, the two-stage melting curve led to two $T_{1/2}$ values, 64 and 80 °C (Figure S4D). A comparison of these results with those of HJ alone indicated that the second denaturing stage in the presence of K^+ is due to the melting of the GQ. Similarly, the $T_{1/2}$ value of GQ in **par(0A)** was found to be 86 °C (Figure S5C), while the GQ in **hyb(0A)** was too stable to lead to a reliable $T_{1/2}$ determination (Figure S5D). The thermal stabilities of all other assemblies were investigated (Figures S6–S8) and support GQ formation in these assemblies.

Molecular Dynamics. To gain further insights into the structure and dynamics of these assemblies, molecular dynamics (MD) simulations were performed. A series of investigations on the HJ-GQ assembly showed that the HJ with attached antiparallel GQ with either abab (**apl(0A)**) or aabb (**apd(0A)**, Figure 3A; of note, all calculated models will be indicated in italic hereafter) strand arrangement was stable (Figure 3A). Steric requirements of the DNA backbone led to unpairing of up to 3 base pairs in the arms adjacent to the GQ, with a greater disruption for **apd** than for **apl**, due to the partial unwinding of arm 2 (Figure S9). This series of MD simulations thus indicated that the HJ-GQ assembly is fully suited for further experimental and theoretical investigations. The **apl(0A)** model allowed to discriminate which strand in the **apl** GQ binds to which strand in HJ: this model showed that the strands P1, P2, P3, and P4 likely progress in the clockwise direction (blue arrow, Figure 3B-F). Given that the strand arrangement in **par** and **hyb** is equivalent to **apl**, we assume their orientation is also clockwise, while the strand progression of the **apd** model seems to resemble a reversed letter "Z": (i.e., "Σ").

GQ/Hemin Interaction. We first investigated the interactions between hemin and HJ-GQ assemblies by UV–vis spectroscopy. The wavelength of the Soret band of hemin was shifted from 398 to 404 nm and its intensity increased after the addition of constrained GQ (Figure S10A). This reflects the disaggregation of hemin upon binding to GQs and the coordination of its iron center to the solvent-exposed G-quartet.[35,36] In comparison, the addition of the HJ alone did not lead to any change in the hemin Soret band (Figure S10A). By titrating the constrained GQs to hemin, their binding affinities could be calculated (Figure S10B) and the association constants (K_a) determined for **apl(0A)**, **par(0A)**, and **hyb(0A)** assemblies were 7.5 ± 0.7, 5.7 ± 0.6, and $6.8 \pm 0.6 \times 10^5$ M^{-1}, respectively. These values being almost equal, they indicate that the affinity of hemin for the 3 GQs is equivalent, demonstrating that the structural differences in the terminal G-quartets of the 3 HJ-GQ assemblies do not affect the binding of hemin, rather unexpectedly.

To further investigate how hemin binds to these assemblies, MD simulations were performed with GQs exhibiting flanking nucleotides, in the absence of HJ. These calculations revealed several possible pathways: (1) a direct binding of hemin to the terminal G-quartet, which is the simplest and commonly accepted mechanism across the GQ models; (2) an indirect binding in which hemin transiently binds to the backbone of a terminal G, before sliding onto the G-quartet; (3) another indirect, less common mechanism, in which hemin binds to the grooves of the GQs before either sliding onto the terminal G-quartet or unbinding from the groove and being released back into the solvent; and finally, (4) a flanking base(s)-assisted binding, which will be further described below.

No systematic differences in the hemin binding mechanism were found between the four investigated GQ topologies, but we observed a dependency on the presence and nature of the flanking nucleotides. The transient hemin binding to a d(A) followed by its transfer to the adjacent G-quartet resembles the binding process we observed for the human telomeric GQ with TTA loops.[37] In systems with flanking 3′-d(TC) and 5′-d(CT), a similar mechanism is possible, in which hemin first binds to either d(C) or d(T) prior to sliding onto the adjacent G-quartet. We also identified a more complex process involving both the flanking bases: after the initial hemin binding to a single flanking base, the nucleotide changed its

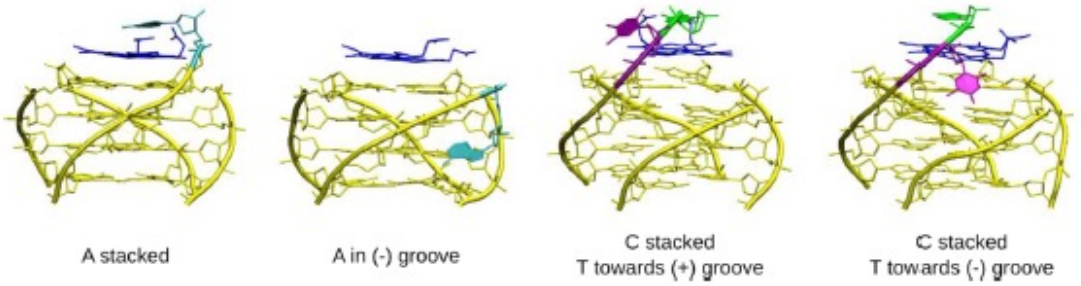

Figure 5. Flanking bases with hemin. Four most common arrangements of flanking bases around G-stem (yellow) with hemin (blue): the flanking d(A) (cyan) prefers to stack above hemin; the flanking d(TC) adopts a conformation in which d(C) (green) stacks onto hemin and d(T) (purple) points toward the adjacent grooves. These figures have been obtained for **par** GQ_1; analogous clusters are found in the **hyb**, **apd**, and **apl** systems.

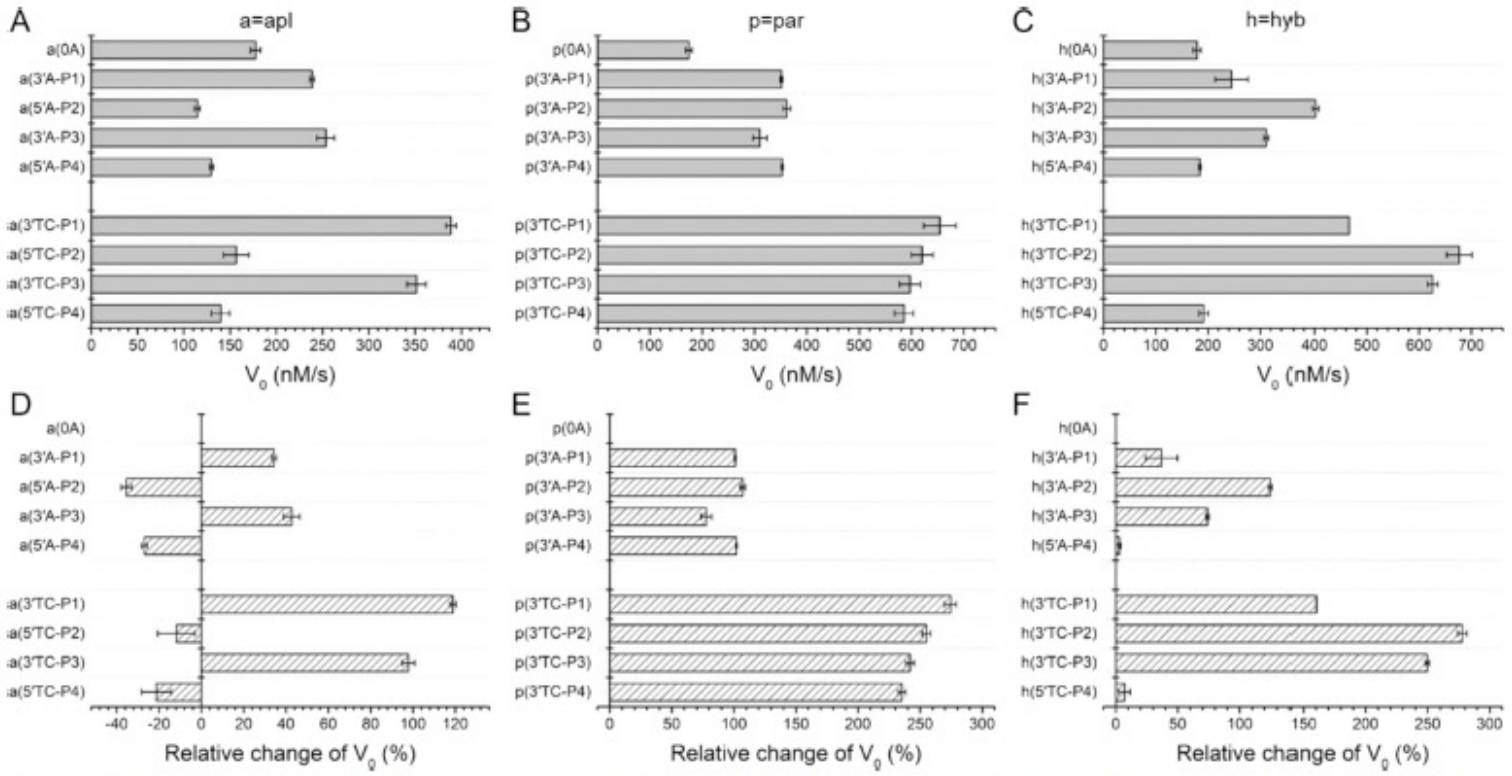

Figure 6. Initial reaction rates of DNAzymes. (A) Antiparallel, (B) parallel, and (C) hybrid GQs ($n = 3$). Relative activity changes that result from the addition of d(A) or d(TC) flanking nucleotides in (D) antiparallel, (E) parallel, and (F) hybrid GQs, compared to the corresponding GQs without any flanking nucleotide.

conformation to form an intermediate in which hemin stacked onto a T=C base pair, whose other face stacked onto the G-stem. This base pair got disrupted and hemin then slid onto the adjacent G-quartet (see the Supporting Movie SBinding). Occasionally, d(C) could stack onto hemin's solvent-exposed face, while d(T) was stacked in between hemin and GQ, so a distinct sandwich structure GQ/d(T)/hemin/d(C) could be transiently formed. This intermediate was in general marginally stable, as hemin could quickly escape from the sandwich and binds directly to the proximal G-quartet. Hemin binding events in all the individual simulations are briefly described in Table S4.

Hemin and G-Stems without Flanking Nucleotides. Hemin always stacked atop the terminal G-quartet of GQs, with the iron aligned with the GQ channel; only minor differences were found between the different topologies (Figure S11). In addition, hemin could rotate about its vertical axis in a manner dependent on the GQ topology: the 2- and 4-fold symmetry in **par(0A)** and **apl(0A)**, respectively (Figure 3), was manifested in hemin rotation phase distribution curves also bearing 2- and 4-fold symmetry, respectively (Figures 4A and S12). In contrast, no such pattern is present in **apd(0A)** nor **hyb(0A)**, which are asymmetric (Figure S12). In **hyb(0A)**, there was a strong preference for a single state in which hemin interacts with the 5′-end sugar moiety; in **apd(0A)**, there were two high, but uneven peaks, which originate in the non-equivalency of the two 5′-end sugar moieties.

Hemin and G-Stems with Flanking Nucleotides. Clustering revealed a few dominant positions of the flanking bases with respect to the G-stem (Table S3, Figure 5): (1) d(A) was dominantly stacked onto hemin so that hemin was sandwiched between d(A) and the G-quartet; (2) a less common conformation had a d(A) lying in the (−) or (+) groove (see Figure 3F for (−) and (+) definition); (3) with d(TC), the dominant conformation is that displaying a d(C) stacked onto hemin and d(T) being aside toward the (−) or (+) groove. The simulations showed that flanking d(A) and d(C), while being stacked onto hemin, positioned their functional groups in the vicinity of the hemin iron as a function of their glycosidic orientation: in the *anti* orientation, N1 and N3 laid above hemin while they are farther in the *syn* conformation, being replaced by the amino group in case of d(A) (Figures 4B and S13). Hemin was also found to be misaligned with the central GQ channel in the *syn*

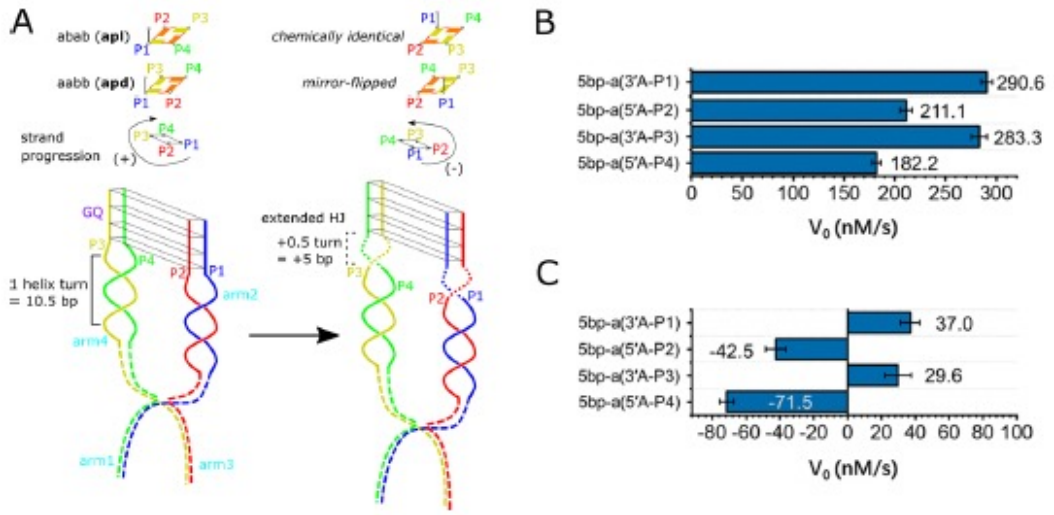

Figure 7. Extended HJ-GQ assembly. (A) Elongation of HJ triggers an inversion of GQ orientation; in the **apl** systems with a tail appended to just one end, the orientation change is only seen in the aabb arrangement. (B) Initial reaction rates of DNAzymes with extended HJ-GQs with antiparallel GQ arrangements. (C) Relative activity changes resulted from the addition of d(A) flanking nucleotides compared to the corresponding GQs without any flanking nucleotide.

conformation (Figure S11). In general, the bases in the 3′-tailed d(A) and d(TC) variants of all the models adopted the *anti* conformation while the 5′-terminal bases adopted the *syn* conformation to various degrees because of an internal H-bond between 5′-OH and the base. For instance, the flanking d(A) in ***apl(5′A-P24)*** often stacked in the *syn* conformation (42%), as well as the d(C) in ***apl(5′TC-P24)*** (25%); the 5′-flanking d(A) had 68 and 64% *syn* population in ***apd(5′A-P2)*** and ***apd(5′A-P4)***, respectively, and the flanking d(C) had a *syn* population of 20 and 35% in the respective d(TC) variants; in ***hyb(5′A-P4)***, d(A) stacked in *syn* conformation (91%) while d(C) in ***hyb(5′TC-P4)*** had also a significant *syn* population (30%).

Catalytic Performance. The catalytic oxidation of 2,2′-azino-bis(3-ethylbenzothiazoline-6-sulfonic acid) (ABTS) by the stochiometric oxidant H_2O_2 is a classical model reaction to assess the performance of GQ DNAzymes. We thus implemented a series of ABTS catalytic oxidations with constrained GQs in interaction with hemin. Initial reaction velocity (V_0) could be obtained by monitoring the formation of the oxidized product $ABTS^{\cdot+}$ (with a typical UV−vis signature at 420 nm) as a function of time (Figure S14). The results are summarized in Figure 6A−C. Briefly, we found that (1) the HJ alone catalyzed ABTS oxidation to a very limited extent (V_0 = 6 nM s^{-1}); (2) all the HJ-GQ assemblies were much more efficient: for the GQs without any tail, activities of **apl**, **par**, and **hyb** GQs were equivalent (V_0 = 175−179 nM s^{-1}); for GQs with a single tail, d(A) or d(TC), the catalytic activity of **par** and **hyb** GQs were higher than those of **apl** GQs, with V_0 = 253, 310, and 311 nM s^{-1} for **apl(3′A-P3)**, **par(3′A-P3)** and **hyb(3′A-P3)**, respectively, and 351, 597, and 626 nM s^{-1} for **apl(3′TC-P3)**, **par(3′TC-P3)**, and **hyb(3′TC-P3)**, respectively. Globally, the addition of a d(TC) tail always led to better catalytic performance than the d(A) tail at the same position for **apl**, **par**, and **hyb** GQs. These results are consistent with our previous data using classical unimolecular parallel GQs.[14]

This series of results revealed an obvious tail position effect as the proximal nucleotide affects the catalytic activity of GQs in a topology-dependent manner. To quantify this effect, the relative reaction rate changes that resulted from the nucleotide tails were calculated (Figure 6D−F): (1) for **apl** GQs, the addition of a d(A) tail at the P2 and P4 positions led to a decrease in the reaction rate by −35 and −27%, respectively, and that of d(TC) by −12 and −21%, respectively; on the contrary, the addition of a d(A) tail at P1 and P3 positions led to a rate increase of 34 and 43%, respectively, and that of d(TC) of 119 and 98%, respectively; (2) for **par** GQs, the addition of either a d(A) or a d(TC) tail at any positions always led to a great rate increase, from 76 up to 269%; (3) for **hyb** GQs, the addition of a d(A) tail at P1, P2, and P3 positions increases the reaction rate by 37 and 124%, respectively, and that of or d(TC) by 160 and 278%, respectively; at the P4 position, the effect is weak (3−7%). This marked tail position effect was confirmed by the catalytic oxidation of 2 other substrates, tyramine and amplex red (Figure S15A,B): the relative rate changes were consistent with that of ABTS (Figures 6D and S15C,D), demonstrating the generality of this effect, which likely originates in the optimization of the hemin binding pocket with the good positioning of the G-quartet, as a proximal ligand, and the nucleotide tail, as a distal ligand of hemin.

The GQ/hemin complex is known to be quickly degraded by the oxidant H_2O_2 in the absence of the ABTS substrate, and this can be monitored by the changes in the porphyrin's Soret band at 404 nm (Figure S16).[14,35,38] The initial degradation rates (V_d) of all the complexes (Figure S17A−C) were thus used as an estimation of the formation rate of the active intermediate species. The V_d values for **apl(0A)**, **par(0A)**, and **hyb(0A)** are all close to 11 nM s^{-1}, indicating that without flanking nucleotides and/or loops, the **apl**, **par**, and **hyb** GQs activate hemin in an equivalent manner. In sharp contrast, the V_d values obtained for the other systems (Figure S17D−F) confirmed the tail position effect: (1) for **apl** GQs, the addition of a d(A) tail at the P2 and P4 positions led to a decrease in the degradation rate by −12 and −26%, while the same tail at the P1 and P3 positions led to an increase in the degradation rate of 30 and 36%; that of d(TC) tail led to a limited change at the P2 position of only 3%; (2) for the **par** and **hyb** GQs, the addition of both d(A) and d(TC) tails at any positions always led to increases in degradation rates. The correlation of V_d as a function of V_0 had an excellent linear correlation (Pearson's r = 0.977, Figure S18). Altogether, these observations confirmed the role that flanking nucleotides

play in the catalytic performance of the resulting GQs, which is found to be dependent on both the nature of the tails (d(A) versus d(TC)) and the topology of the GQs, which are uniquely and fully harnessed here, thanks to the HJ-mediated topological control of GQ conformation.

HJ as a Modulator of the GQ Orientation. We finally decided to further exploit the unique structural possibilities offered by the HJ template in the control of the GQ orientation. Indeed, as discussed above, **apl** GQs offer the most complex picture because of their two possible arrangements referred to as **apl** and **apd** (Figure 3). Even if the simplified model seen in Figure 1 suggests that the **apl** orientation is the privileged GQ topology, MD simulations of the HJ-GQ assembly of **apl(0A)** and **apd(0A)** suggest that this structure could be a mixture of the two arrangements. To investigate this in more detail, we had a closer look to these models: **apl** displays equivalent 3′- and 5′-ends, while **apd** has four nonequivalent ends, as confirmed during MD simulations. Even if the catalytic properties of all **apl** GQs were found to be roughly similar, the slight difference observed between P1- versus P3- and P2- versus P4-tailed sequences deserved to be better rationalized. To this end, we measured the catalytic activities of a modified HJ-GQ assembly in which the HJ arms connected to an **apl** GQ with a d(A) tail were extended by five base pairs (Tables S5 and S6), corresponding to half a turn of the double helix (Figure 7A). The stability of this extended HJ-GQ assembly was experimentally verified (Figures S19 and S20).

This modification should in theory lead to an inversed direction of strand progression of the formed GQ: therefore, the extended P1-tailed sequence would catalytically behave like the previous P3-tailed sequence and vice versa; similarly, the extended P2-tailed sequence would behave like the previous P4-tailed sequence and vice versa. Importantly, the singly tailed **apl** arrangement should be insensitive to this orientation inversion and no change in catalytic behavior is expected because of the 2-fold symmetry of the **apl** GQ (Figure 7A); in contrast, the **apd** arrangement being nonsymmetrical, a P1 ↔ P3 and P2 ↔ P4 swaps should be observed when measuring the catalytic activities. We indeed experimentally determined such a swap (Figure 7B,C; to be compared with Figure 6A,D); from this observation, we concluded that (1) the **apd** arrangement is present in the sample, even if we cannot determine its exact ratio; however, given the better way in which the **apl** arrangement fits to the HJ in MD simulations, we can reasonably postulate that the ratio of **apd** is weak; (2) more globally, these results showed that the GQ orientation could be driven by the length of the connecting HJ arms; we hypothesize that the balance between the **apl** and **apd** populations is controlled by the global twist of the duplex arms, which is itself controlled by their length. The balance between the **apl** and **apd** populations thus relies on the global twist of the HJ double-helical arms, perhaps in a sine wave-like manner, reflecting the twist's periodic nature.

■ DISCUSSION

The microenvironment of the catalytic center of an enzyme is critical for its function. In the case of horseradish peroxidase (HRP)-mimicking GQ-based DNAzymes, the binding pocket of hemin within the GQ structure comprises the terminal G-quartet of the GQ, which acts as a proximal ligand for the hemin's iron center, and the flanking nucleotides that surround the accessible G-quartet (d(A), d(TC) or d(CT) here), which act as distal ligands of hemin's Fe atom. The presence of these nucleotides is critical as they assist the cleavage of the stoichiometric oxidant H_2O_2 to form the active intermediate. Synergic effects between these proximal and distal ligands determine the catalytic performance of the corresponding GQs.

GQs used as pre-catalysts can be either parallel (**par**), hybrid (**hyb**) or antiparallel (**apl**) GQs. They fold intramolecularly, which creates surrounding loops: in **hyb** and **apl** GQs, these loops could be either lateral or diagonal loops that span through the terminal G-quartets and could thus impair the proper stacking of hemin atop the GQ's G-quartet; in **par** GQs, loops are propeller loops that span through the GQ grooves, which should not alter hemin binding. It is therefore not easy to compare the catalytic activity of **apl**, **par**, and **hyb** GQs: to make such a comparison possible and relevant, we provide here a unique approach in which we constrained tetramolecular GQs with **apl**, **par**, and **hyb** topologies without any loop, using a Holliday junction (HJ) template. This approach allows for fully controlling both the GQ topology and hemin binding, thus addressing a conundrum raised by previous studies using either zippered GQs[15] or covalent GQ/hemin systems,[39,40] with which no GQ topology-dependent differences in catalytic performances were observed. Here, we add another level of control, precisely positioning activating tails and assessing the consequences of their presence and nature on the catalytic properties of the resulting GQs.

Our results show that **apl**, **par**, and **hyb** GQs without any tail equivalently bind to and activate hemin (Figures 6, S10 and S17). They also show that the influence of the surrounding nucleotides (or tails) is critical: to understand the molecular basis of this finding, we performed MD simulations and found that (1) the binding modes of hemin to tailless **apl(0A)**, **apd(0A)**, **par(0A)**, and **hyb(0A)** were similar: when stacked atop the terminal G-quartet, the iron atom of hemin was mostly aligned with the GQ channel (Figure S11). Thus, the lack of difference in hemin binding among the GQ topologies provides a rationale for their similar catalytic activity (Figure 6); (2) there is an obvious correlation between the observed catalytic activity of d(A)- and d(TC)-tailed GQs and the population of d(A)'s N1 or d(C)'s N3 (atoms of key importance in the catalytic cycle) in vicinity of Fe in MD simulations for all the studied topologies (Table S3 and Figure S13); and (3) the 5′-d(A) tail adopts a significant population of the *syn* conformation because of the formation of an internal 5′-OH···N1 H-bond.[41] This results either in an unfavorable orientation of N1 (Figure S13) or in a misalignment of hemin with respect to the G-stem channel. The effect of the *syn* conformation occurs to a smaller extent in 5′-d(CT) too. From these structural observations, we can thus postulate the following catalytic activity order: 3′-d(TC) > 3′-d(A) > unmodified GQ ≥ 5′-d(CT) ≥ 5′-d(A), an order that was fully confirmed by our experiments (Figure 6).

The differences in activities between the same flanking nucleotides at different positions on a given GQ are harder to explain, although MD simulations provide some insights into nonparallel GQ. In the **hyb** models with 3′-flanking nucleotides, the strands P1, P2, and P3 have different adjacent grooves, which affects the way the flanking nucleotides interact with hemin. Even if some notable differences were obtained in the pattern of 2D-restricted radial distribution function (RDF*, detailed in the Supporting Information, Figure S13), it would be speculative to explain mechanistically the

difference in the catalytic activity between the models, yet the simulations were able to capture the difference between hybrid GQs tailed at P1 versus P2 versus P3, which was confirmed by the experiments. For the **apl** GQs, the situation is more complex, given the co-existence of the **apl** and **apd** models. We showed and discussed above that both the MD calculations and the experimental results obtained with HJ-GQ constructs with different HJ arm lengths confirmed that the two systems do indeed co-exist in solution, in a ratio that remains to be determined accurately. This new approach, based on the modulation of the HJ arm length to seize control over the GQ orientation, is highly versatile and must now be extended to other GQ topologies in order to precisely assess its actual scope. Some limitations deserve however to be highlighted, such as the fact that the presence of HJ precludes the access of the second GQ's G-quartet, thus decreasing the number of DNAzyme active centers and also that this suprastructure may affect somehow the flexibility of the GQ DNAzyme, which may preclude optimal access of the substrate to the catalytic center. However, it is clear from that series of results that controlling the precise nature of the hemin binding pocket within GQs is possible by incorporating GQs into a HJ-based suprastructure. This strategy, combined with in-depth MD simulations and experimental analyses, confirms that (1) the terminal G-quartets of **apl**, **par**, and **hyb** GQs are equivalent for both activation of and binding to hemin and (2) the proximal nucleotides govern the activation of and binding to hemin, in a manner that is dependent on both the GQ topology and position of the flanking nucleotides. By doing so, we keep on optimizing the catalytic properties of GQ-based systems with the hope of bringing them even closer to their natural enzymatic counterparts.

MATERIAL AND METHODS

Oligonucleotides and Reagents. Ultra-PAGE or HPLC-purified oligonucleotides were purchased from Sangon Biotech (Shanghai, China) without further purification, and sequences are provided in Tables S1 and S5. The oligonucleotides were dissolved in ultrapure water (18.2 MΩ cm) and strand concentrations were determined by using UV absorbance at 260 nm with the molar extinction coefficient provided by the manufacturer. Hemin (iron(III)-protoporphyrin IX, ≥98%) was dissolved in DMSO, diluted to 0.1 mM, and then stored in the dark at 4 °C. Freshly prepared 2,2′-azino-bis(3-ethylbenzothiazoline-6-sulfonic acid) (ABTS, ≥98%) was dissolved in ultrapure water to 50 mM. H_2O_2 was freshly prepared by directly diluting the high concentration H_2O_2 of 30% v/v (~10 M) to 50 mM in ultrapure water prior to use. All chemicals were obtained from Sigma-Aldrich.

General Procedure for DNA Hybridization. The first step for the formation of HJ constrained GQ (Step 1, Figure 1C) involved mixing equimolar amounts of oligodeoxynucleotide strands P1–P4 (10 μM) in 12 mM Tris–HCl buffer (pH 7.0) in the presence of 120 mM LiCl and subsequent annealing by heating to 95 °C for 5 min and then cooling slowly to 25 °C. In the second step (Step 2, Figure 1C), the assemblies were diluted to 8 μM final concentration of oligodeoxynucleotides in 10 mM Tris–HCl buffer (pH 7.0) in the presence of 150 mM KCl and 120 mM LiCl, then incubated at 4 °C for 48 h to let the GQ fold completely and kept at 25 °C for 0.5 h before measurements.

Isothermal Difference Spectra (IDS). UV absorption spectra were recorded between 220 and 350 nm at 25 °C on an Agilent Cary 100 spectrophotometer equipped with a Peltier temperature controller.[33] First, the spectrum of the DNA assembly sample in 10 mM Tris–HCl buffer (pH 7.0) supplemented with 120 mM LiCl only was recorded after the abovementioned Step 1. Then, 150 mM KCl was added and a second spectrum was recorded after a 48 h incubation to allow proper GQ assembly. As KCl addition induces a change in volume, spectra are corrected for dilution.

UV Melting. DNA assemblies (2.0 μM) dissolved in 10 mM Tris–HCl buffer (pH 7.0) containing 120 mM LiCl without and with 150 mM KCl were placed in a stoppered quartz cuvette of 1 cm path length, and then, thermal denaturation was performed using an Agilent Cary 100 spectrophotometer equipped with a Peltier effect heated cuvette holder. Absorbance at 260 nm and 295 nm within a temperature range of 5–95 °C was monitored at a fixed heating rate of 0.5 °C/min.

Circular Dichroism. CD spectra of DNA assemblies (2 μM) dissolved in 10 mM Tris–HCl buffer (pH 7.0) containing 120 mM LiCl without and with 150 mM KCl were collected on a Chirascan circular spectropolarimeter (Applied Photophysics) between 220 and 350 nm. The lamp was kept under a stable stream of dry purified nitrogen (99.9%) during experiments, and the measurements were repeated in triplicate at 25 °C.

Dissociation Constant (K_d) Determination. To evaluate the binding affinity between DNA assembly and hemin, the absorption spectra of hemin with increasing concentrations of DNA were recorded. Prior to the measurement, 2 μM hemin was incubated with 0 to 4 μM DNA assembly in 10 mM Tris–HCl buffer (pH 7.0) containing both 120 mM LiCl and 150 mM KCl at 25 °C for 2 h. Spectra from 370 to 550 nm were collected on a Agilent Cary100 spectrophotometer at 25 °C. The saturation curves for the binding of hemin with GQs were determined by plotting the fraction of bound hemin (α, determined by eq 1) as a function of DNA concentration and fitting with a one-site binding model, using a software of GraphPad Prism 5, to extract the dissociation constant K_d value:

$$\alpha = \frac{A_x - A_0}{A_\infty - A_0} \quad (1)$$

where A_x is the absorbance at 404 nm for complex of hemin and DNA with different concentrations, A_∞ and A_0 are the absorbances in the presence of saturating DNA and in the absence of DNA, respectively. Association constant K_a = [GQ/hemin]/[GQ][hemin] is defined as the reciprocal of K_d on the basis of $K_a{}^*K_d = 1$.

Models for MD Simulations. The computational investigation of hemin interactions with the HJ-GQ assembly was divided into two parts. The first one was focused on the interaction of hemin with GQ, leaving the HJ away, making these computations straightforward and affordable. The second one, more computationally demanding, dealt with the structural stability of the HJ-GQ assembly. The interaction of hemin with GQ was studied on several G-stem topologies and flanking nucleotides (Figure 3). Four distinct G-stems were investigated: (i) parallel topology with all Gs in the *anti* orientation (**par**). The starting structure of this G-stem was taken from the X-ray structure of tetramolecular parallel GQ $d(TGGGGT)_4$ (PDB ID: 352D).[42] (ii) 3 + 1 hybrid topology (**hyb**) with *syn-anti-syn-anti* arrangement of guanines in the

individual strands. The model was constructed by taking two quartets from the 3 + 1 hybrid human telomeric G-quadruplex (PDB ID: 2GKU)[43] and subsequent merger of two such two-quartet subunits. (iii) 2 + 2 antiparallel topology with adjacent strands of the opposite direction, i.e., the abab arrangement (**apl**), constructed by merging of two 15-thrombin-binding aptamer G-stems (PDB ID: 148D).[44] (iv) 2 + 2 antiparallel topology with one adjacent strand parallel and one in the opposite direction, i.e., the aabb arrangement (**apd**), taken from the X-ray structure of the *O. nova* telomeric sequence $d(T_4G_4T_4)_2$ (PDB ID: 1JPQ).[45] The merging was done in Swiss-PdbViewer[46] and the xleap module of AMBER.[47] The four G-stem topologies were studied in contexts of three various flanking sequences, following the experimental setup: (i) completely truncated, i.e., no flanking nucleotides were present; (ii) single dA appended to the 3′-end or 5′-end of one G-strand, (iii) d(TC) dinucleotide appended to the 3′-end of one G-strand or d(CT) dinucleotide appended to the 5′-end of one G-strand (Figure 3). Note that (a)symmetries of the individual G-stems allow for different numbers of stereochemically unique 3′ and 5′-terminal positions. Note also that both the terminal G-quartets of **apl** and **apd** are stereochemically identical, which allowed for adding flanking nucleotides to both sides of the G-stem, so that we obtained two independent, yet chemically equivalent hemin binding sites in one model, which increased the computational efficiency. To study the hemin binding mechanism and hemin binding modes, the GQ models were simulated together with hemin. In the case of truncated GQs, hemin was placed in proximity of the terminal G-quartet it should bind to. For models with flanking nucleotides, hemin was placed up to 20 Å away from GQ (measured between centers of mass) and binding to G-stem was achieved during classical MD simulations. Five different starting positions of hemin were generated for each system. We created three HJ-GQ assembly models: two with **apl(0A)** and one with **apd(0A)** GQ (Figure 3). The models were constructed by taking a HJ core, which was then extended by canonical double-helices and attaching the **apl** or **apd** GQ to two of the helices; the nucleotide sequence was identical to the experimental setup. **Par** and **hyb** GQs within the HJ-GQ assembly were not tested because they would require additional force field parametrization for the strand inversion. The model structures after equilibration are enclosed in the Supporting Information as a PDB file.

MD Simulations. We performed explicit solvent MD simulations of the GQ models binding hemin and HJ-GQ systems using the parmOL15 force field[47] (which includes earlier force field modifications[48−52] for DNA and GAFF)[53] for hemin, carried out in AMBER18[47] (see the Supporting Information for more details). The performance of the parmOL15 force field has been recently extensively verified against HJ crystal structures.[54] We tried two different parameter sets for hemin and each model was run at least 5 times to obtain independent trajectories. The list of all simulations with their briefly described outcome is in Table S4. Altogether, we performed 361 independent simulations with a total cumulative time of 1311 μs.

Analysis. For each model, we concatenated the parts of independent trajectories that had hemin bound to the terminal quartet, took a frame every 5 ns, and performed clustering by RMSD by the density peak algorithm with a local distance cutoff of 1 Å and cluster centers having a density of at least 100.[55] We have also defined and measured three distribution functions: (i) hemin rotation phase distribution, where the rotation phase is a measure describing relative orientation of rotating stacked hemin with respect to the G-stem at a given moment; (ii) distribution of hemin Fe to carbonyl O6 distances for guanines in the quartet binding hemin, to evaluate the (mis)alignment of hemin iron with the G-stem channel; (iii) tailored radial distribution function of hemin Fe to heteroatoms and centroid of the six-membered ring in tailed d(A) and d(TC), which tells us which atoms of the flanking base are closer to Fe and which are farther. More details about the analysis method are provided in the Supporting Information.

DNAzyme Activity and GQ/Hemin Complex Degradation Measurement. The DNA assemblies (1.0 μM) were incubated with hemin (2.0 μM) in 10 mM Tris−HCl buffer (pH 7.0) containing 0.05% (v/v) Triton X-100, 2%(v/v) DMSO, 150 mM KCl, and 120 mM LiCl for 2 h at 25 °C. For the activity assay, the substrate (ABTS at a final concentration of 0.6 mM) and H_2O_2 (0.6 mM) were added sequentially. Product formation was followed by monitoring the absorbance of $ABTS^{\cdot+}$ using an Agilent Cary100 spectrophotometer for 60 s using extinction coefficients of 36,000 M^{-1} cm^{-1} for $ABTS^{\cdot+}$ at 420 nm. The initial rate (V_0, nM/s) of the oxidation reaction was obtained from the slope of the initial linear portion (the first 10 s) of the plot of absorbance versus reaction time by using eq 2. For the degradation measurement, absorbance of the Soret band (404 nm) of the GQ/hemin complex was recorded after 0.6 mM H_2O_2 was added (no ABTS added). Initial degradation velocity (V_d) was obtained from the slope of the initial linear portion (the first 5 s) by using the following eq 3.

$$V_0 = \frac{|dC_{ABTS^{\cdot+}}|}{dt} = \frac{|dA_{ABTS^{\cdot+}}|}{dt \times b \times \varepsilon_{ABTS^{\cdot+}}} \quad (2)$$

$$V_d = \frac{|dC_{complex}|}{dt} = \frac{|dA_{complex}|}{dt \times b \times \varepsilon_{complex}} \quad (3)$$

where $C_{ABTS^{\cdot+}}$ and $C_{complex}$ are the real-time concentrations of oxidation product $ABTS^{\cdot+}$ and GQ/hemin complex, respectively; t is the reaction time; A is the absorbance of $ABTS^{\cdot+}$ at λ = 420 nm and complex at λ = 404 nm, respectively; b is the light path length, which is 1.0 cm; ε are the molar extinction coefficient of $ABTS^{\cdot+}$ at λ = 420 nm and GQ/hemin complex at λ = 404 nm, respectively. Each measurement was repeated in triplicate.

■ ASSOCIATED CONTENT

Supporting Information

MD simulation details; additional MD results; additional references (PDF)

Supporting movie SBinding (MP4)

Models of HJ-GQ construct (PDB)

Hemin parameter files for AMBER (ZIP)

■ AUTHOR INFORMATION

Corresponding Authors

Petr Stadlbauer − *Institute of Biophysics of the Czech Academy of Sciences, 612 00 Brno, Czech Republic;*

orcid.org/0000-0002-5470-8376; Email: stadlbauer@ibp.cz

David Monchaud – *Institut de Chimie Moléculaire (ICMUB), CNRS UMR6302, Université de Bourgogne, 21078 Dijon, France;* orcid.org/0000-0002-3056-9295; Email: david.monchaud@u-bourgogne.fr

Jun Zhou – *State Key Laboratory of Analytical Chemistry for Life Science, School of Chemistry & Chemical Engineering, Nanjing University, Nanjing 210023, China;* orcid.org/0000-0002-6793-3169; Email: jun.zhou@nju.edu.cn

Authors

Dehui Qiu – *State Key Laboratory of Analytical Chemistry for Life Science, School of Chemistry & Chemical Engineering, Nanjing University, Nanjing 210023, China*

Mingpan Cheng – *School of Engineering, China Pharmaceutical University, Nanjing 211198, China;* orcid.org/0000-0003-1282-0076

Jielin Chen – *State Key Laboratory of Analytical Chemistry for Life Science, School of Chemistry & Chemical Engineering, Nanjing University, Nanjing 210023, China;* orcid.org/0000-0003-4930-2870

Michal Langer – *Regional Centre of Advanced Technologies and Materials, Czech Advanced Technology and Research Institute (CATRIN), Palacký University Olomouc, 783 71 Olomouc, Czech Republic; Chemical and Biological Systems Simulation Lab, Centre of New Technologies University of Warsaw, 02-097 Warszawa, Poland*

Xiaobo Zhang – *State Key Laboratory of Analytical Chemistry for Life Science, School of Chemistry & Chemical Engineering, Nanjing University, Nanjing 210023, China;* orcid.org/0000-0003-0222-2515

Qiang Gao – *CAS Key Lab of Low-Carbon Conversion Science and Engineering, Shanghai Advanced Research Institute, Chinese Academy of Sciences, Shanghai 201210, China;* orcid.org/0000-0002-8783-3245

Huangxian Ju – *State Key Laboratory of Analytical Chemistry for Life Science, School of Chemistry & Chemical Engineering, Nanjing University, Nanjing 210023, China;* orcid.org/0000-0002-6741-5302

Jiří Šponer – *Institute of Biophysics of the Czech Academy of Sciences, 612 00 Brno, Czech Republic;* orcid.org/0000-0001-6558-6186

Jean-Louis Mergny – *State Key Laboratory of Analytical Chemistry for Life Science, School of Chemistry & Chemical Engineering, Nanjing University, Nanjing 210023, China; Institute of Biophysics of the Czech Academy of Sciences, 612 00 Brno, Czech Republic; Laboratoire d'Optique et Biosciences, Ecole Polytechnique, CNRS, INSERM, Institut Polytechnique de Paris, 91120 Palaiseau, France;* orcid.org/0000-0003-3043-8401

Author Contributions

◆D.Q., M.C., and P.S. contributed equally to this work.

Notes

The authors declare no competing financial interest.

■ ACKNOWLEDGMENTS

This work was supported by the National Natural Science Foundation of China (21977045, 22177047, 22004062, and 22104063), the State Key Laboratory of Analytical Chemistry for Life Science (5431ZZXM2202, SKLACLS2109, and SKLACLS2307), the Fundamental Research Funds for the Central Universities (020514380299, 202200324, and 202200325), China Postdoctoral Science Foundation (2021 M702106), ANR grant ANR-21-CE44-0005-01 "ICARE," Scientific Research Foundation for High-level Faculty, China Pharmaceutical University (3150110048), Shanghai Pujiang Program (20PJ1415200), Special Project for Peak Carbon Dioxide Emissions-Carbon Neutrality (21DZ1206900) from the Shanghai Municipal Science and Technology Commission, the Double First-Rate construction plan of China Pharmaceutical University (CPU2022QZ14), the Czech Science Foundation to J. S. and P. S. (21-23718S), and the Symbit project (Reg. no. CZ.02.1.01/0.0/0.0/15 003/0000477) financed by the ERDF (to J.S. and J.L.M.). P.S. acknowledges the use of CESNET data storage facilities (LM2018140).

■ REFERENCES

(1) Breaker, R. R.; Joyce, G. F. A DNA enzyme that cleaves RNA. *Chem. Biol.* **1994**, *1*, 223–229.

(2) Silverman, S. K. Catalytic DNA: scope, applications, and biochemistry of deoxyribozymes. *Trends Biochem. Sci.* **2016**, *41*, 595–609.

(3) Sen, D.; Poon, L. C. H. RNA and DNA complexes with hemin [Fe(III) heme] are efficient peroxidases and peroxygenases: how do they do it and what does it mean? *Crit. Rev. Biochem. Mol. Biol.* **2011**, *46*, 478–492.

(4) Yum, J. H.; Park, S.; Sugiyama, H. G-quadruplexes as versatile scaffolds for catalysis. *Org. Biomol. Chem.* **2019**, *17*, 9547–9561.

(5) Mergny, J. L.; Sen, D. DNA quadruple helices in nanotechnology. *Chem. Rev.* **2019**, *119*, 6290–6325.

(6) Shumayrikh, N. M.; Warren, J. J.; Bennet, A. J.; Sen, D. A heme•DNAzyme activated by hydrogen peroxide catalytically oxidizes thioethers by direct oxygen atom transfer rather than by a Compound I-like intermediate. *Nucleic Acids Res.* **2021**, *49*, 1803–1815.

(7) Cheng, X.; Liu, X.; Bing, T.; Cao, Z.; Shangguan, D. General peroxidase activity of G-quadruplex-hemin complexes and its application in ligand screening. *Biochemistry* **2009**, *48*, 7817–7823.

(8) Kong, D. M.; Cai, L. L.; Guo, J. H.; Wu, J.; Shen, H. X. Characterization of the G-quadruplex structure of a catalytic DNA with peroxidase activity. *Biopolymers* **2009**, *91*, 331–339.

(9) Li, T.; Dong, S.; Wang, E. G-quadruplex aptamers with peroxidase-like DNAzyme functions: which is the best and how does it work? *Chem. – Asian J.* **2009**, *4*, 918–922.

(10) Nakayama, S.; Sintim, H. O. Colorimetric split G-quadruplex probes for nucleic acid sensing: improving reconstituted DNAzyme's catalytic efficiency via probe remodeling. *J. Am. Chem. Soc.* **2009**, *131*, 10320–10333.

(11) Chang, T.; Gong, H.; Ding, P.; Liu, X.; Li, W.; Bing, T.; Cao, Z.; Shangguan, D. Activity enhancement of G-quadruplex/hemin DNAzyme by flanking d(CCC). *Chem. – Eur. J.* **2016**, *22*, 4015–4021.

(12) Li, W.; Li, Y.; Liu, Z.; Lin, B.; Yi, H.; Xu, F.; Nie, Z.; Yao, S. Insight into G-quadruplex-hemin DNAzyme/RNAzyme: adjacent adenine as the intramolecular species for remarkable enhancement of enzymatic activity. *Nucleic Acids Res.* **2016**, *44*, 7373–7384.

(13) Guo, Y.; Chen, J.; Cheng, M.; Monchaud, D.; Zhou, J.; Ju, H. A thermophilic tetramolecular G-quadruplex/hemin DNAzyme. *Angew. Chem., Int. Ed.* **2017**, *56*, 16636–16640.

(14) Wang, J.; Cheng, M.; Chen, J.; Ju, H.; Monchaud, D.; Mergny, J. L.; Zhou, J. An oxidatively damaged G-quadruplex/hemin DNAzyme. *Chem. Commun.* **2020**, *56*, 1839–1842.

(15) Li, J.; Wu, H.; Yan, Y.; Yuan, T.; Shu, Y.; Gao, X.; Zhang, L.; Li, S.; Ding, S.; Cheng, W. Zippered G-quadruplex/hemin DNAzyme: exceptional catalyst for universal bioanalytical applications. *Nucleic Acids Res.* **2021**, *49*, 13031–13044.

(16) Li, W.; Chen, S.; Xu, D.; Wen, Q.; Yang, T.; Liu, J. A DNA as a substrate and an enzyme: direct profiling of methyltransferase activity by cytosine methylation of a DNAzyme. *Chem. – Eur. J.* **2018**, *24*, 14500–14505.
(17) Chen, J.; Wang, J.; van der Lubbe, S. C. C.; Cheng, M.; Qiu, D.; Monchaud, D.; Mergny, J.-L.; Guerra, C. F.; Ju, H.; Zhou, J. A push–pull mechanism helps design highly competent G-quadruplex-DNA catalysts. *CCS Chem.* **2021**, *3*, 2183–2193.
(18) Cheng, M.; Zhou, J.; Jia, G.; Ai, X.; Mergny, J. L.; Li, C. Relations between the loop transposition of DNA G-quadruplex and the catalytic function of DNAzyme. *Biochim. Biophys. Acta, Gen. Subj.* **2017**, *1861*, 1913–1920.
(19) Chen, J.; Zhang, Y.; Cheng, M.; Guo, Y.; Šponer, J.; Monchaud, D.; Mergny, J.-L.; Ju, H.; Zhou, J. How proximal nucleobases regulate the catalytic activity of G-quadruplex-hemin DNAzymes. *ACS Catal.* **2018**, *8*, 11352–11361.
(20) Chen, J.; Guo, Y.; Zhou, J.; Ju, H. The effect of adenine repeats on G-quadruplex/hemin peroxidase mimicking DNAzyme activity. *Chem. – Eur. J.* **2017**, *23*, 4210–4215.
(21) Stefan, L.; Denat, F.; Monchaud, D. Deciphering the DNAzyme activity of multimeric quadruplexes: insights into their actual role in the telomerase activity evaluation assay. *J. Am. Chem. Soc.* **2011**, *133*, 20405–20415.
(22) Stefan, L.; Denat, F.; Monchaud, D. Insights into how nucleotide supplements enhance the peroxidase-mimicking DNAzyme activity of the G-quadruplex/hemin system. *Nucleic Acids Res.* **2012**, *40*, 8759–8772.
(23) Cao, Y.; Li, W.; Gao, T.; Ding, P.; Pei, R. One Terminal guanosine flip of intramolecular parallel G-quadruplex: catalytic enhancement of G-quadruplex/hemin DNAzymes. *Chem. – Eur. J.* **2020**, *26*, 8631–8638.
(24) Cheng, Y.; Cheng, M.; Hao, J.; Jia, G.; Monchaud, D.; Li, C. The noncovalent dimerization of a G-quadruplex/hemin DNAzyme improves its biocatalytic properties. *Chem. Sci.* **2020**, *11*, 8846–8853.
(25) Golub, E.; Albada, H. B.; Liao, W. C.; Biniuri, Y.; Willner, I. Nucleoapzymes: hemin/G-quadruplex DNAzyme-aptamer binding site conjugates with superior enzyme-like catalytic functions. *J. Am. Chem. Soc.* **2016**, *138*, 164–172.
(26) Aleman Garcia, M. A.; Hu, Y.; Willner, I. Switchable supramolecular catalysis using DNA-templated scaffolds. *Chem. Commun.* **2016**, *52*, 2153–2156.
(27) Albada, H. B.; Golub, E.; Willner, I. Rational design of supramolecular hemin/G-quadruplex-dopamine aptamer nucleoapzyme systems with superior catalytic performance. *Chem. Sci.* **2016**, *7*, 3092–3101.
(28) Shumayrikh, N.; Huang, Y. C.; Sen, D. Heme activation by DNA: isoguanine pentaplexes, but not quadruplexes, bind heme and enhance its oxidative activity. *Nucleic Acids Res.* **2015**, *43*, 4191–4201.
(29) Lustgarten, O.; Carmieli, R.; Motiei, L.; Margulies, D. A molecular secret sharing scheme. *Angew. Chem., Int. Ed.* **2019**, *58*, 184–188.
(30) Chen, J.; Cheng, M.; Wang, J.; Qiu, D.; Monchaud, D.; Mergny, J. L.; Ju, H.; Zhou, J. The catalytic properties of DNA G-quadruplexes rely on their structural integrity. *Chin. J. Catal.* **2021**, *42*, 1102–1107.
(31) Guedin, A.; Lin, L. Y.; Armane, S.; Lacroix, L.; Mergny, J. L.; Thore, S.; Yatsunyk, L. A. Quadruplexes in 'Dicty': crystal structure of a four-quartet G-quadruplex formed by G-rich motif found in the Dictyostelium discoideum genome. *Nucleic Acids Res.* **2018**, *46*, 5297–5307.
(32) Cheng, M.; Hao, J.; Li, Y.; Cheng, Y.; Jia, G.; Zhou, J.; Li, C. Probing the interaction of copper cofactor and azachalcone substrate with G-quadruplex of DNA based Diels-Alderase by site-specific fluorescence quenching titration. *Biochimie* **2018**, *146*, 20–27.
(33) Mergny, J. L.; Li, J.; Lacroix, L.; Amrane, S.; Chaires, J. B. Thermal difference spectra: A specific signature for nucleic acid structures. *Nucleic Acids Res.* **2005**, 33, No. e138.
(34) Del Villar-Guerra, R.; Trent, J. O.; Chaires, J. B. G-quadruplex secondary structure obtained from circular dichroism spectroscopy. *Angew. Chem., Int. Ed.* **2018**, *57*, 7171–7175.
(35) Travascio, P.; Witting, P. K.; Mauk, A. G.; Sen, D. The peroxidase activity of a hemin-DNA oligonucleotide complex: free radical damage to specific guanine bases of the DNA. *J. Am. Chem. Soc.* **2001**, *123*, 1337–1348.
(36) Travascio, P.; Li, Y.; Sen, D. DNA-enhanced peroxidase activity of a DNA aptamer-hemin complex. *Chem. Biol.* **1998**, *5*, 505–517.
(37) Stadlbauer, P.; Islam, B.; Otyepka, M.; Chen, J.; Monchaud, D.; Zhou, J.; Mergny, J. L.; Sponer, J. Insights into G-quadruplex-hemin dynamics using atomistic simulations: implications for reactivity and folding. *J. Chem. Theory Comput.* **2021**, *17*, 1883–1899.
(38) Yang, X.; Fang, C.; Mei, H.; Chang, T.; Cao, Z.; Shangguan, D. Characterization of G-quadruplex/hemin peroxidase: substrate specificity and inactivation kinetics. *Chem. – Eur. J.* **2011**, *17*, 14475–14484.
(39) Kosman, J.; Zukowski, K.; Juskowiak, B. Comparison of characteristics and DNAzyme activity of G4–Hemin conjugates obtained via two Hemin attachment methods. *Molecules* **2018**, *23*, 1400.
(40) Chen, Y.; Qiu, D.; Zhang, X.; Liu, Y.; Cheng, M.; Lei, J.; Mergny, J.; Ju, H.; Zhou, J. Highly sensitive biosensing applications of a magnetically immobilizable covalent G-Quadruplex-Hemin DNAzyme catalytic system. *Anal. Chem.* **2022**, *94*, 2212–2219.
(41) Cang, X.; Sponer, J.; Cheatham, T. E. Explaining the varied glycosidic conformational, G-tract length and sequence preferences for anti-parallel G-quadruplexes. *Nucleic Acids Res.* **2011**, *39*, 4499–4512.
(42) Phillips, K.; Dauter, Z.; Murchie, A. I.; Lilley, D. M.; Luisi, B. The crystal structure of a parallel-stranded guanine tetraplex at 0.95 Å resolution. *J. Mol. Biol.* **1997**, *273*, 171–182.
(43) Luu, K. N.; Phan, A. T.; Kuryavyi, V.; Lacroix, L.; Patel, D. J. Structure of the human telomere in K^+ solution: an intramolecular (3 + 1) G-quadruplex scaffold. *J. Am. Chem. Soc.* **2006**, *128*, 9963–9970.
(44) Schultze, P.; Macaya, R. F.; Feigon, J. Three-dimensional solution structure of the thrombin-binding DNA aptamer d-(GGTTGGTGTGGTTGG). *J. Mol. Biol.* **1994**, *235*, 1532–1547.
(45) Haider, S.; Parkinson, G. N.; Neidle, S. Crystal structure of the potassium form of an oxytricha nova G-quadruplex. *J. Mol. Biol.* **2002**, *320*, 189–200.
(46) Guex, N.; Peitsch, M. C. SWISS-MODEL and the Swiss-PdbViewer: An environment for comparative protein modeling. *Electrophoresis* **1997**, *18*, 2714–2723.
(47) Case, D. A.; et al. *AMBER 18*; University of California: San Francisco, 2018.
(48) Zgarbova, M.; Sponer, J.; Otyepka, M.; Cheatham, T. E., 3rd; Galindo-Murillo, R.; Jurecka, P. Refinement of the sugar-phosphate backbone torsion beta for AMBER force fields improves the description of Z- and B-DNA. *J. Chem. Theory Comput.* **2015**, *11*, 5723–5736.
(49) Perez, A.; Marchan, I.; Svozil, D.; Sponer, J.; Cheatham, T. E., 3rd; Laughton, C. A.; Orozco, M. Refinement of the AMBER force field for nucleic acids: improving the description of alpha/gamma conformers. *Biophys. J.* **2007**, *92*, 3817–3829.
(50) Krepl, M.; Zgarbova, M.; Stadlbauer, P.; Otyepka, M.; Banas, P.; Koca, J.; Cheatham, T. E., 3rd; Jurecka, P.; Sponer, J. Reference simulations of noncanonical nucleic acids with different chi variants of the AMBER force field: quadruplex DNA, quadruplex RNA and Z-DNA. *J. Chem. Theory Comput.* **2012**, *8*, 2506–2520.
(51) Zgarbova, M.; Luque, F. J.; Sponer, J.; Cheatham, T. E., 3rd; Otyepka, M.; Jurecka, P. Toward improved description of DNA backbone: revisiting epsilon and zeta torsion force field parameters. *J. Chem. Theory Comput.* **2013**, *9*, 2339–2354.
(52) Cornell, W. D.; Cieplak, P.; Bayly, C. I.; Gould, I. R.; Merz, K. M.; Ferguson, D. M.; Spellmeyer, D. C.; Fox, T.; Caldwell, J. W.; Kollman, P. A. A second generation force field for the simulation of proteins, nucleic acids, and organic molecules. *J. Am. Chem. Soc.* **2002**, *117*, 5179–5197.

(53) Wang, J.; Wolf, R. M.; Caldwell, J. W.; Kollman, P. A.; Case, D. A. Development and testing of a general amber force field. *J. Comput. Chem.* **2004**, *25*, 1157−1174.
(54) Simmons, C. R.; MacCulloch, T.; Krepl, M.; Matthies, M.; Buchberger, A.; Crawford, I.; Sponer, J.; Sulc, P.; Stephanopoulos, N.; Yan, H. The influence of Holliday junction sequence and dynamics on DNA crystal self-assembly. *Nat. Commun.* **2022**, *13*, 3112.
(55) Rodriguez, A.; Laio, A. Machine learning. Clustering by fast search and find of density peaks. *Science* **2014**, *344*, 1492−1496.